POLITECNICO DI TORINO
Repository ISTITUZIONALE

Blind test comparison of wave–structure interactions: A non-linear Froude–Krylov modelling approach

(Article begins on next page)

21 December 2022

ice | **proceedings**

Blind test comparison of wave-structure interactions: A non-linear Froude-Krylov modelling approach

Giuseppe Giorgi
Post-doc researcher, Department of Mechanical and Aerospace
Engineering, Politecnico di Torino, Turin, Italy

One of the essential stepping stones for reaching economic viability and industrial feasibility of the wave energy conversion sector is the effectiveness of the device design, which is dependent, among others, to the accuracy of mathematical models used for development. Despite being more than 45 years old, modelling is not mature yet and there is still a clear lack of standardization of modelling techniques, and a need for increasing confidence in hydrodynamic models. The objective of the the Collaborative Computational Project in Wave Structure Interaction (CCP-WSI) is to critically compare and evaluate various different modelling techniques, under the same shared experimental conditions, and using clearly pre-defined metrics. This paper details a contribution implementing, in a computationally efficient way, nonlinear Froude-Krylov forces and nonlinear kinematics. The goal is to define a medium-high fidelity model, higher than linear models and comparable with nonlinear models, but able to compute at a small fraction of the computational time typically required by fully-nonlinear models. The case study considers survivability-like wave conditions, represented by three steep focused waves, which are particularly challenging to be modelled using partially-nonlinear potential theory-based mathematical models. Despite a poor representation in the pitch and surge response, a good agreement with experimental heave response and mooring load is found, at small computation time (compared to fully-nonlinear models), close to real-time computation.

1. Introduction

The current market of renewable and sustainable energy generation is increasingly crowded and competitive, so that developers of wave energy converter (WEC) technology are required to systematically reduce the cost of energy and attain economic viability. One of the major challenges developers of wave energy conversion systems have to face, both in design and optimization stages, is the relatively low trust in their mathematical models. The effectiveness of the power generation and control strategy strongly depends on the fidelity of the model (Giorgi and Ringwood, 2018a,e; Ringwood et al., 2018). Furthermore, reliable prediction

of structural loads is mandatory to assure security of personnel and integrity of components, while avoiding over-sizing of the structure and excessive safety coefficients.

Despite the "modelling problem" of wave energy converters being at least 45 years old (Salter, 1974), it still can hardly be defined matured or settled. In fact, early linear models, reasonably borrowed from conventional ocean engineering where the objective is usually to stabilize the floater, are often inadequate to fit the wave energy problem, since motion enhancement and power absorption maximization are naturally defying the linearity assumption.

However, although the inclusion of nonlinearities has effectively the potential to increase the model representativeness, it also usually demands the toll of additional complexity, and therefore computational burden. The consequent dilemma of finding the best compromise between model accuracy and computational time fostered, in recent years, the generation of a large number of nonlinear models (Davidson and Costello, 2020). The performance of each model strongly depends on the device operative principle (Wang *et al.*, 2019), dimension (Clément and Ferrant, 1988), shape (Penalba *et al.*, 2017), installation site (Giorgi and Ringwood, 2018f), and operational condition (Giorgi and Ringwood, 2018b). Moreover, there are different fidelity/computational requirements according to the application of the model (i.e. design, model-based control, simulation, survivability, etc.). Therefore, it is extremely challenging to define a level playing field of comparison between different modelling approaches that could fairly, systematically and substantially evaluate which model is best for what. Recent years have witnessed the pressing need for consistent model evaluation and standardization (Ransley *et al.*, 2016), and a common endeavour from several different players seems to be an effective way to share efforts, avoid the danger of personal bias, and increase the data basin and model diversity while having one common case study (Ransley *et al.*, 2019). This trend lead to a modelling competition (Garcia-Rosa *et al.*, 2015), the IEA-OES project (Wendt *et al.*, 2019) and, finally, the present CCP-WSI project, which this work is part of (Ransley *et al.*, 2020a,b). These collaborative projects have the common objective of comparing different modelling approaches for a given test case. While both (Garcia-Rosa *et al.*, 2015) and (Ransley *et al.*, 2020a,b) are blind tests, (Wendt *et al.*, 2019) fully discloses all experimental data from the start. On the other hand, (Wendt *et al.*, 2019) provides a wider range of tests (free decay, diffraction test, radiation test, and response to regular and irregular waves), but for a single-degree of freedom device.

One peculiar characteristic of the CCP-WSI Blind-Test series 2 and 3 (BT2 and BT3, respectively) is the unavailability of the experimental results at the moment of submission, so tuning the model based on the expected results is not possible. Both BT2 and BT3 consider focused waves for the same couple of buoys, one with hemispherical bottom and one with a moonpool, but using different wave characteristics (constant height in BT2 and constant steepness in BT3). The CCP-WSI Blind-Test series 3 took place during the

29th International International Offshore and Polar Engineering Conference (ISOPE-2019) (Giorgi, 2019b), while the CCP-WSI Blind-Test series 2 took place during the 13th European Wave and Tidal Energy Conference (EWTEC-2019) (Giorgi, 2019a). The blind test comparison was done with the blind submissions, so that participants were not able to tune their results as part of the tests. After the conference, however, the full experimental data was released, allowing participants to compare their simulations and potentially revise or tune their model.

The present paper uses the provided experimental data to evaluate and discuss on the accuracy of the modelling approach proposed for CCP-WSI-BT2 (Giorgi, 2019a), with the novelty being the comparison with experimental results and discussion of accuracy and sources of error. The modelling approach examined in this paper is based on partially-nonlinear potential theory, with the inclusion of nonlinear kinematics (Fossen, 2011) and analytical nonlinear Froude-Krylov (FK) forces (Giorgi *et al.*, 2020). Such a model purports to achieve a higher level of accuracy (compared to a fully-linear model) at a small fraction of the computational time required by fully-nonlinear models. Note that, although experimental data was available at the moment this paper was written, the results herein provided are unchanged from the ones in (Giorgi, 2019a). In fact, as further discussed in Sect. 2, this model is fully based on first principles and no tuning parameter is present, so it is not possible to change the results to better fit the benchmarking experimental data.

Finally, the reader is invited to download and test the open-source **NLFK demonstration toolbox**, openly available at (Giorgi, 2019c).

2. Equation of motion

Wave-structure interactions and nonlinear floater kinematics and dynamics are conveniently described in two different frames of reference, as shown in Fig. 1. The first one is an inertial frame (x, y, z), with x along and concordant with the positive wave propagation direction, z vertical and positive upwards, y according to the right-hand rule, and the origin at the centroid of the water plane area of the floater in static equilibrium. Since its directions

are constant in time, this frame is best used to keep track of the floater displacement $\boldsymbol{\zeta}$:

$$(1) \quad \boldsymbol{\zeta} = \begin{bmatrix} \mathbf{p} \\ \boldsymbol{\Theta} \end{bmatrix} \quad , \quad \mathbf{p} = \begin{bmatrix} x \\ y \\ z \end{bmatrix} \quad , \quad \boldsymbol{\Theta} = \begin{bmatrix} \phi \\ \theta \\ \psi \end{bmatrix},$$

where $\mathbf{p}$ represents linear positions (surge, sway, and heave), and $\boldsymbol{\Theta}$ represents angular positions (roll, pitch, and yaw). However, it is convenient to formulate the dynamic equation of motion in a body-fixed frame $(\hat{x}, \hat{y}, \hat{z})$, so that moments of inertia are time-invariant. Furthermore, if the centre of gravity (CoG) is chosen as the origin of the body-fixed frame, such moments of inertia are minimal and the inertia matrix is diagonal.
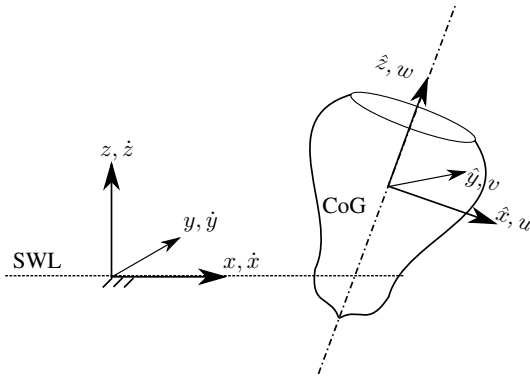

Figure 1. Inertial frame (x, y, z), with the origin at still water level (SWL), and body-fixed (non-inertial) frame $(\hat{x}, \hat{y}, \hat{z})$, with the origin at the centre of gravity (CoG) of the body. Velocities according to the inertial frame $(\dot{x}, \dot{y}, \dot{z})$ and the body-fixed frame (u, v, w)

However, since the body-fixed frame is rotating (hence accelerating) with the body, non-inertial effects should be taken into account, namely Coriolis and centripetal forces. Newton's equation of motion is defined according to the floater velocity $\boldsymbol{\nu}$, expressed in the body-fixed frame:

$$(2) \quad \boldsymbol{\nu} = \begin{bmatrix} \mathbf{v} \\ \boldsymbol{\omega} \end{bmatrix} \quad , \quad \mathbf{v} = \begin{bmatrix} u \\ v \\ w \end{bmatrix} \quad , \quad \boldsymbol{\omega} = \begin{bmatrix} p \\ q \\ r \end{bmatrix}$$

where $\boldsymbol{\nu}$ represents linear velocities and $\boldsymbol{\omega}$ represents angular velocities.

The rate of change of displacements in the global frame $(\dot{\boldsymbol{\zeta}})$ is computed from the body velocities $(\boldsymbol{\nu})$ by means a transformation matrix $(\mathbf{J}_{\boldsymbol{\Theta}})$, depending on the instantaneous angular orientation of the body-fixed frame with respect to the inertial frame $(\boldsymbol{\Theta})$. Please refer to Sect. 2.2 for further details. Therefore, displacement and velocity of the body are computed by solving the following set of first-order differential equations:

$$(3) \quad \begin{cases} \dot{\boldsymbol{\zeta}} = \mathbf{J}_{\boldsymbol{\Theta}} \boldsymbol{\nu} \\ \mathbf{M}\dot{\boldsymbol{\nu}} + \mathbf{C}_{Cor}\boldsymbol{\nu} = \mathbf{F}_d + \mathbf{F}_{FK} + \mathbf{F}_{rad} + \mathbf{F}_{moor}, \end{cases}$$

where $\mathbf{M}$ is the inertial matrix, $\mathbf{F}_{Cor} = \mathbf{C}_{Cor}\boldsymbol{\nu}$ is the Coriolis/centripetal force, $\mathbf{F}_d$ is the linear diffraction force, $\mathbf{F}_{rad}$ is the radiation force, and $\mathbf{F}_{moor}$ is the mooring force. Note that $\mathbf{F} \in \mathbb{R}^6$ is a generalized force, composed of a linear force vector $\mathbf{f} \in \mathbb{R}^3$, and a torque vector $\boldsymbol{\tau} \in \mathbb{R}^3$.

Furthermore, note that no viscous term is present in the equation of motion (3), since the model is based on the inviscid potential flow theory. It would be possible to artificially include viscous effects by means of a Morison-like term (Bhinder *et al.*, 2011), but a drag coefficient should be identified, ideally using experimental data. However, in blind-test comparisons as well as in usual preliminary design or shape optimization applications, there is no experimental data to reliably identify the drag coefficient. Therefore, viscous effects have been neglected. Consequently, this model cannot be adjusted according to better fit experimental data, since it is based on first principles and no tuning parameter is present. In particular, results provided in Sect. 4 have not been modified after that the experimental data has been released, maintaining the blind-test condition valid. Indeed, one of the main objectives of this paper is to produce and evaluate a model fully-based on first principles and with no tuning factor. Nevertheless, a sensitivity analysis on the drag coefficient is provided in (Giorgi, 2019a) for the geometry with sharp edges (more affected by viscous losses) showing, as expected, a decrease of the response.

Considering the body to be small compared to the typical wavelength, it is reasonable to assume linear diffraction and radiation forces (Clément and Ferrant, 1988). Furthermore, by means of a moment-matching identification technique it is possible to replace the radiation convolution integral by a more computationally convenient state space representation (Faedo *et al.*, 2018). On the other hand, since large motions are expected from a wave energy converter in order to maximize power absorption, the following nonlinearities should be considered:

■ nonlinear FK forces, due to large translational and rotational displacements, making variations of the instantaneous wetted surface significant (see Sect. 2.1).

■ nonlinear kinematics, due to large rotational displacements and velocities (see Sect. 2.2);

2.1. Nonlinear Froude-Krylov force

Froude-Krylov forces are defined as the integral of the undisturbed pressure field (P) over the wetted surface of the floater, plus the gravity force. In the linear approximation, it is assumed that the relative motion between the body and the free surface is small, so that FK forces are computed with respect to the mean wetted surface. On the contrary, nonlinear FK force calculations are performed with respect to the actual *instantaneous* wetted surface ($S_w(t)$):

$$(4a) \quad \mathbf{f}_{FK} = \mathbf{f}_g + \iint_{S_w(t)} P\mathbf{n}\, dS,$$

$$(4b) \quad \boldsymbol{\tau}_{FK} = \mathbf{r}_g \times \mathbf{f}_g + \iint_{S_w(t)} P\mathbf{r} \times \mathbf{n}\, dS,$$

where $\mathbf{f}_g$ is the gravity force, $\mathbf{n}$ is the unity vector normal to the surface, $\mathbf{r}$ is the generic position vector, and $\mathbf{r}_g$ is the position vector of the CoG. The undisturbed incident pressure field of uni-directional regular wave is defined as:

$$(5) \quad P(x,z,t) = -\rho g z + a \cos(\omega t - kx) \frac{\cosh(k(z'+h))}{\cosh(kh)},$$

where a, ω, and k are the wave amplitude, frequency, and number, respectively, ρ the water density, g the acceleration of gravity, h the water depth, and z' the vertical coordinate modified according to Wheeler's stretching (Giorgi and Ringwood, 2018f). Stretching techniques are a pragmatic way to reduce the impact of errors due to violations of the free surface boundary conditions of linear potential flow approaches, which are particularly detrimental when NLFK forces are computed at high positive peaks. Although they always improve Airy's theory results in computing NLFK forces(Giorgi and Ringwood, 2018f), their accuracy in represent the pressure field decays with the degree of nonlinearity of the wave, namely with its steepness. Therefore, due to the particularly steep focused waves considered in this study, inaccuracies of the pressure field description can be expected.

Solving integrals in (4) requires, in general, computationally demanding mesh-based approaches (Gilloteaux, 2007). However, more computationally convenient methods are attainable for axisymmetric bodies (Giorgi and Ringwood, 2018c), taking advantage of cylindrical coordinates (ϱ, ϑ) to obtain an analytical representation of the wetted surface:

$$(6) \quad \begin{cases} \hat{x}(\varrho,\vartheta) = f(\varrho)\cos\vartheta \\ \hat{y}(\varrho,\vartheta) = f(\varrho)\sin\vartheta \\ \hat{z}(\varrho,\vartheta) = \varrho \end{cases}, \quad \vartheta \in [-\pi,\pi) \wedge \varrho \in [\varrho_1, \varrho_2]$$

where $f(\varrho)$ is a generic function of the vertical coordinate ϱ, describing the profile of revolution of the axisymmetric body. Since it is convenient to define the FK integrals in the body-fixed frame of reference, the pressure field must be mapped from the inertial to the body-fixed frame. Therefore, after some manipulations (Giorgi and Ringwood, 2018d), the integral in (4a), for example, becomes:

$$\mathbf{f}_{FK} = \mathbf{R}_\Theta^T \mathbf{f}_g + \iint_{S_w(t)} P(\hat{x},\hat{y},\hat{z})\mathbf{n}\, dS =$$

$$(7) \quad = \mathbf{R}_\Theta^T \mathbf{f}_g + \int_{-\pi}^{\pi} \int_{\varrho_1}^{\varrho_2} P(\varrho,\vartheta)(\mathbf{e}_\varrho \times \mathbf{e}_\vartheta)\, d\varrho d\vartheta,$$

where $\mathbf{e}_\varrho$ and $\mathbf{e}_\vartheta$ are the unity vector along ϱ and ϑ, respectively. Note that the transpose of rotation matrix is used to map the gravity force in the body-fixed frame. The integral in (7) is solved numerically, using a 2D-quadrature scheme for trapezoidal integration.

2.2. Nonlinear kinematics

Let us define, for convenience of notation, the skew-symmetric operator $\mathcal{S} : \mathbb{R}^3 \to \mathbb{R}^{3\times3}$ as

$$(8) \quad \mathcal{S} : \left\{ \boldsymbol{\lambda} \in \mathbb{R}^3 \,\middle|\, \mathcal{S}(\boldsymbol{\lambda}) \triangleq \begin{bmatrix} 0 & -\lambda_3 & \lambda_2 \\ \lambda_3 & 0 & -\lambda_1 \\ -\lambda_2 & \lambda_1 & 0 \end{bmatrix} \right\}.$$

It follows that $\mathcal{S}(\boldsymbol{\lambda}) = -\mathcal{S}(\boldsymbol{\lambda})^T$, and that the cross-product can be written as:

$$(9) \quad \boldsymbol{\lambda} \times \mathbf{a} = \mathcal{S}(\boldsymbol{\lambda})\mathbf{a}$$

Since the equation of motion is described in a rotating (hence accelerating) frame of reference, Coriolis and centripetal effects should be taken into account. When defined about the CoG, these are computed as follows (Fossen, 2011):

$$(10) \quad \mathbf{F}_{Cor} = \mathbf{C}_{Cor}\boldsymbol{\nu} = \begin{bmatrix} m\mathcal{S}(\boldsymbol{\omega}) & \mathbf{0}_{3\times3} \\ \mathbf{0}_{3\times3} & -\mathcal{S}(\mathbf{I}_g\boldsymbol{\omega}) \end{bmatrix} \begin{bmatrix} \mathbf{v} \\ \boldsymbol{\omega} \end{bmatrix},$$

where m is the mass of the body, and $\mathbf{I}_g$ is the matrix of the moments of inertia with respect to CoG.

Instantaneous velocities generate infinitesimal displacements along the body-fixed axis, which are continuously changing direction in time. Therefore, it is necessary to determine the rate of change of

the displacements ($\dot{\boldsymbol{\zeta}}$) in the global coordinate system by applying the following instantaneous rotations to $\boldsymbol{\nu}$:

$$(11) \quad \dot{\boldsymbol{\zeta}} = \begin{bmatrix} \dot{\mathbf{p}} \\ \dot{\boldsymbol{\Theta}} \end{bmatrix} = \begin{bmatrix} \mathbf{R}_{\boldsymbol{\Theta}} & \mathbf{0}_{3\times3} \\ \mathbf{0}_{3\times3} & \mathbf{T}_{\boldsymbol{\Theta}} \end{bmatrix} \begin{bmatrix} \mathbf{v} \\ \boldsymbol{\omega} \end{bmatrix} = \mathbf{J}_{\boldsymbol{\Theta}}\boldsymbol{\nu},$$

where $\mathbf{R}_{\boldsymbol{\Theta}}$ is the rotation matrix, depending on the Euler angles $\boldsymbol{\Theta}$, defined according to the 3-2-1 convention as:

$$\mathbf{R}_{\boldsymbol{\Theta}} = \mathbf{R}_{\hat{z},\psi}\mathbf{R}_{\hat{y},\theta}\mathbf{R}_{\hat{x},\phi}$$

$$(12) \quad = \begin{bmatrix} c\psi & -s\psi & 0 \\ s\psi & c\psi & 0 \\ 0 & 0 & 1 \end{bmatrix} \begin{bmatrix} c\theta & 0 & s\theta \\ 0 & 1 & 0 \\ -s\theta & 0 & c\theta \end{bmatrix} \begin{bmatrix} 1 & 0 & 0 \\ 0 & c\phi & -s\phi \\ 0 & s\phi & c\phi \end{bmatrix},$$

with c and s standing for $\cos()$ and $\sin()$ trigonometric operators, respectively. $\mathbf{R}_{\boldsymbol{\Theta}}$ is applied to translational velocities, and $\mathbf{T}_{\boldsymbol{\Theta}}$ is applied to rotational ones and is defined as follows:

$$(13) \quad \mathbf{T}_{\boldsymbol{\Theta}} = \begin{bmatrix} 1 & s\phi \cdot t\theta & c\phi \cdot t\theta \\ 0 & c\phi & -s\phi \\ 0 & s\phi/c\theta & c\phi/c\theta \end{bmatrix},$$

where t stands for the $\tan()$ trigonometric operator. Note that the singularity of $\mathbf{T}_{\boldsymbol{\Theta}}$ in $\pm\pi/2$ is usually not an issue in wave energy applications, since the amplitude of the pitch angle is, by design, always expected to be smaller than $\pi/2$.

Note that, if small angular velocities and displacement are assumed (as in the usual linear approximation), Coriolis-centripetal forces in (10) are negligible, and $\mathbf{J}_{\boldsymbol{\Theta}}$ in (11) becomes the identity matrix. Consequently, displacement according to inertial and non-inertial frames are equivalent (Fossen, 2011). However, in this paper such an approximation is rejected, since large pitch angles are expected.

3. Wave tank experiments

The CCP-WSI Blind Test Series 2 focuses on the study hydrodynamic interactions between small bodies and large, steep waves, in order to be representative of point-absorbing WECs in harsh sea states, which can be considered across of the limit of power production region. All details of the experimental campaign are given in (Ransley *et al.*, 2020a). Focused waves are a compact solution to replicate, in the typically short time windows of wave tank experiment, extreme wave conditions equivalent to the highest wave in a long realization of a panchromatic wave. The NewWave theory (Tromans *et al.*, 1991) is applied to a Pierson-Moskowitz spectrum (significant wave height H_s), so that all frequency components arrive with zero phase angle at the focus location, where the device is placed. Three waves are considered, with the same amplitude (A) but increasing peak frequency (f_p), hence steepness (kA), which is a proxy of nonlinearity. Table 1 tabulates waves characteristics and identification codes (ID), while Fig. 2 shows the time traces, only in the time window considered for the comparison, between 35.3s and 50.3s. In the simulations performed for this work, the components of the free surface elevation have been reconstructed from data collected by a wave gauge at the centre of the wave tank (where the device is placed), during a test without the device (empty-tank test). Frequency components have been computed by applying a fast-Fourier transform to filtered and windowed data, and applying a cut-off frequency of 14 rad·s^{-1}.

Table 1. Blind test 2 (BT2) incident wave identification number (ID), amplitude (A), peak frequency (f_p), significant wave height of the original Pierson-Moskowitz spectrum (H_s), and wave steepness (kA).

ID	A [m]	f_p [Hz]	H_s [m]	kA
1BT2	0.25	0.3578	3.0	0.128778
2BT2	0.25	0.4000	3.0	0.160972
3BT2	0.25	0.4382	3.0	0.193167

Two surface-piercing structures have been considered, whose shape and dimensions, compared to the wave length, are characteristic of typical wave energy converters. Two geometries are considered: one hemispherical-bottomed cylinder (G_1), and a cylinder with a moon-pool (G_2). Figure 3 shows the cross-sections of the two geometries, along with dimensions (in mm) and position with respect to the still water level (SWL). Table 2 tabulates the mass and moments of
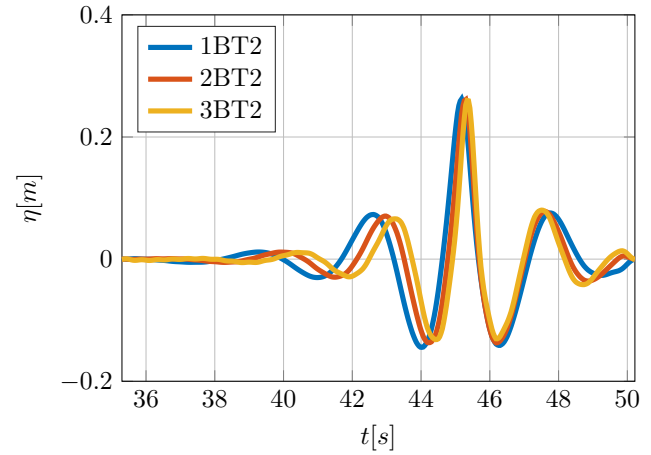

Figure 2. Incident free surface elevation in the time window considered for the analysis.

inertia of the two bodies. Both floaters are moored to the tank floor (water depth 3m) by means of a single pre-tensioned mooring line.

Table 2. Mass and inertia of the two floaters

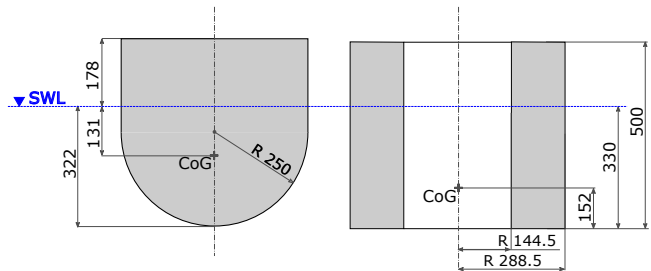|	$M[kg]$	$I_{xx}[kgm^2]$	$I_{yy}[kgm^2]$	$I_{zz}[kgm^2]$
G_1	43.674	1.620	1.620	1.143
G_2	61.459	3.560	3.560	3.298

Figure 3. Dimensions and position (in mm) with respect to the still water level (SWL) of the cross-section of geometry G_1, at the left, and G_2, at the right.

The mooring system is composed of a single line, anchored at the tank floor and attached at the bottom of the device, as shown in Fig. 4. The axial stiffness K_{moor} is the same for both geometries, and equal to 67Nm; the rest length (L_0) is 2.212m for G_1, and 2.204m for G_2. Note that, in order to guarantee correct equilibrium in the mathematical simulation, the rest length has been computed from experimental measurements (mass, draft, mooring

line stiffness, and water density) and from the submerged volume calculated within the NLFK framework. Thanks to the universal joint connecting the mooring line to the floater, $\mathbf{f}_{moor}$ is generally not aligned to the buoy axis, hence $\boldsymbol{\tau}_{moor}$ is not zero. Therefore, the mooring force is computed, in the body-fixed frame, as follows:

$$(14) \quad \mathbf{F}_{moor} = \begin{bmatrix} \mathbf{f}_{moor} \\ \boldsymbol{\tau}_{moor} \end{bmatrix} = \begin{bmatrix} \mathbf{e}_m K_{moor} \Delta L \\ \mathbf{r}_b \times \mathbf{f}_{moor} \end{bmatrix}$$

where $\mathbf{e}_m$ is the unit vector of the mooring line and $\mathbf{r}_b$ is the position of the attach point of the mooring line at the bottom of the floater, both defined with respect to the body-fixed frame.
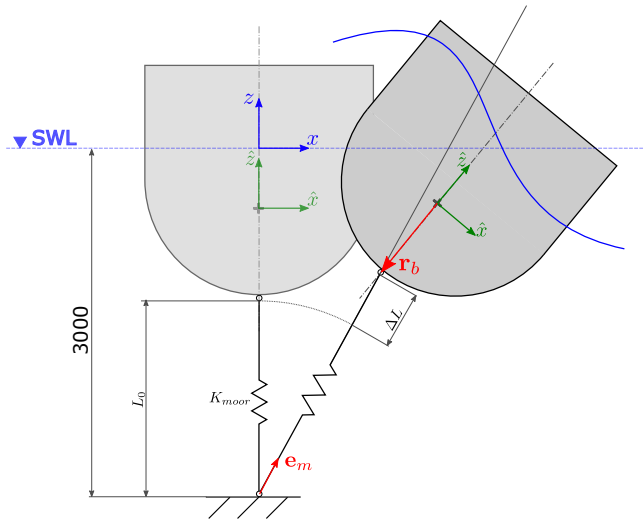
Figure 4. Global and body-fixed frames of reference, shown at the static equilibrium (left) and in operation (right). Schematics of the mooring system, with initial length (L_0) and axial stiffness (K_{moor}) defining the pretension, and line extension ΔL. $\mathbf{e}_m$ is the unit vector of the mooring line and $\mathbf{r}_b$ is the position of the attach point of the mooring line at the bottom of the floater. Water depth shown in mm.

4. Results

A first numerical test that can be performed to support and validate the modelling approach is to compute the dynamic FK forces using linear and nonlinear approaches, but under linear conditions, so that the results should overlap with virtually no error. Such linear conditions refer to zero displacement and a wave amplitude negligible with respect to the freeboard of the floater.

In this case 1mm-wave amplitude is used, which is two orders of magnitude smaller than the freeboard and draft of both geometries. Note that even for the highest considered frequency (15rad/s), the ratio between wave amplitude (1mm) and wavelength is less than 0.4%. For each frequency, a time domain simulation is performed. Once the transient is fully elapsed, it is possible to measure the amplitude of the response and the phase difference with respect to the free surface elevation. Figure 5 shows, for geometry G_1, a successful comparison between the NLFK model and the linear results obtained via the Boundary Element Method (BEM) software Wamit (WAMIT Inc., 2014).

A further test that can be done in order to verify the correctness of the implementation, is to compute the response amplitude operator (RAO), which is the complex ratio between the displacement and the incoming wave. On the one hand, the RAO is directly computed using the frequency domain parameters from a BEM software. On the other hand, a time domain model is defined and solved through a second-order Runge-Kutta scheme. Under linear conditions (1mm-amplitude wave and linear moorings) and using an appropriately small time step, time-domain and frequency-domain results should overlap. Furthermore, the time-domain model is run with and without the inclusion of nonlinearities to further verify the model. Figures 6 and 7 show this overlap for geometries G_1 and G_2, respectively.

The constant time step used for the Runge-Kutta integration scheme can be defined such that a satisfactory trade-off between accuracy and computational effort is obtained. Considering, for example, the response of geometry G_1 to the harsher wave 3BT2, Fig. 8 shows the relative computational time (t_r) and the percentage error (ε) depending on the time step dt, where ϵ is defined as:

$$(15) \quad \varepsilon = mean\left(rms\left(\frac{|\boldsymbol{\zeta} - \boldsymbol{\zeta}_{ref}|}{\boldsymbol{\zeta}_{ref}^{max}} \right) \right)$$

where $\boldsymbol{\zeta}$ is the time dependent vector of the 6-DoF displacements, as defined in (1). $\boldsymbol{\zeta}_{ref}$ is the benchmarking response, obtained for the smallest dt, and $\boldsymbol{\zeta}_{ref}^{max}$ is the maximum of $\boldsymbol{\zeta}_{ref}$. Note that a single value for ε is obtained, as the mean of the errors in surge, heave, and pitch. The computational time is normalized against the time required when the smallest dt is used. By setting an arbitrary
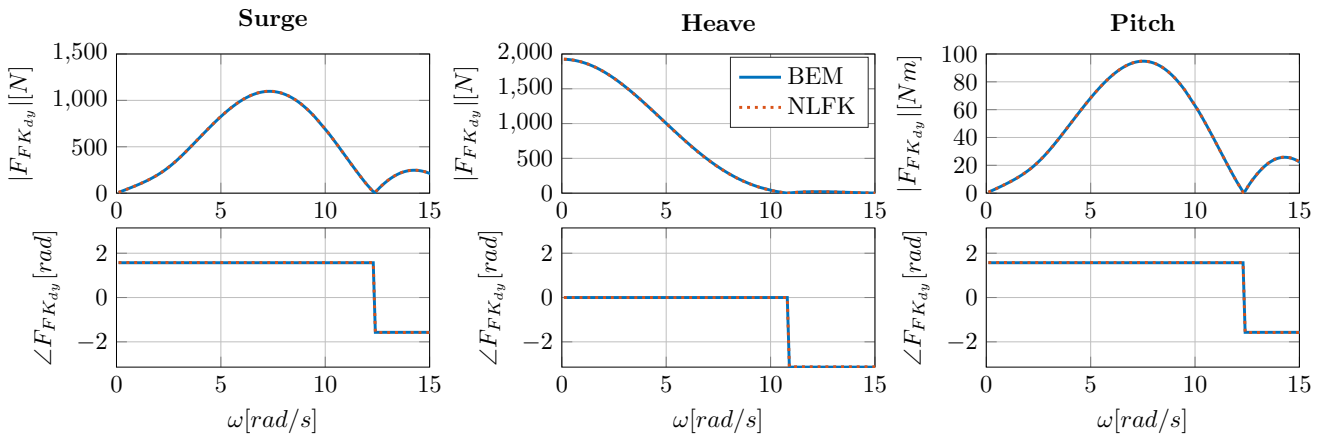
Figure 5. Comparison between dynamic Froude-Krylov force ($F_{FK_{dy}}$) for geometry G_1, computed with a BEM code and the NLFK model in linear conditions, i.e. fixed body and 1mm-amplitude waves.
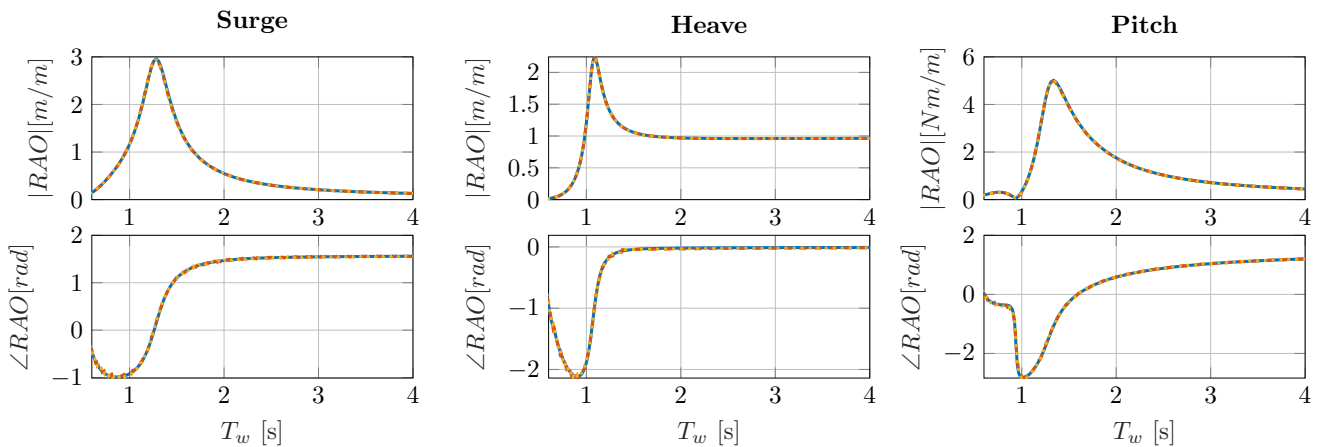

Figure 6. Response amplitude operator for geometry G_1, computed in linear conditions (1mm wave height and linear moorings) in the time domain using a fully-linear (▪▪▪) and a nonlinear (▪▪▪) model, successfully compared to frequency domain calculations (▬).

threshold of $\varepsilon = 1\%$, a time step of 0.04s is selected. Note that (15) performs the average of the error for the three DoFs because ε is a single metric to measure convergence of the whole model, rather than an accuracy metric.The resulting computational time, for both geometries and all waves, is Tabulated in Table 3. The algorithm is implemented in *ad hoc* Matlab code, and run on a single processor of a standard computer (Dell, Precision T5810, Intel® Xeon® CPU E5-1620v3 @ 3.50GHz; RAM:16GB). Table 3 tabulates the normalized computational time, defined as the ratio between run-time and simulation time, so that the real-time computation requirement translates into a normalized time less or

equal than one. Overall, the NLFK model computes from 4.6 to 13.2 times slower than real time. However, considering that this implementation was not optimized for computational speed, and that Matlab is inherently 1 to 2 orders of magnitude slower than lower level coding languages, such as C or Fortran (Wendt *et al.*, 2019), real-time computation is potentially an easily achievable goal. This makes the NLFK model a suitable option for studies requiring computational time of the same order or magnitude of the simulated time.

Analysing Table 3 in more detail, it can be remarked that G_2 is more time-demanding than G_1. On the one hand, G_1 can be
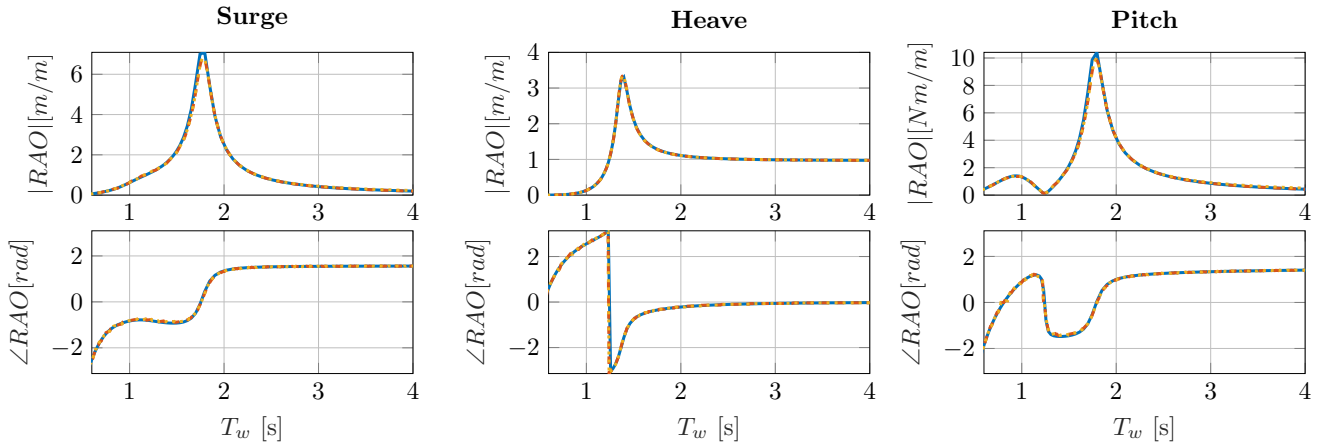
Figure 7. Response amplitude operator for geometry G_2, computed in linear conditions (1mm wave height and linear moorings) in the time domain using a fully-linear (▪▪▪) and a nonlinear (▪▪▪) model, successfully compared to frequency domain calculations (▬).
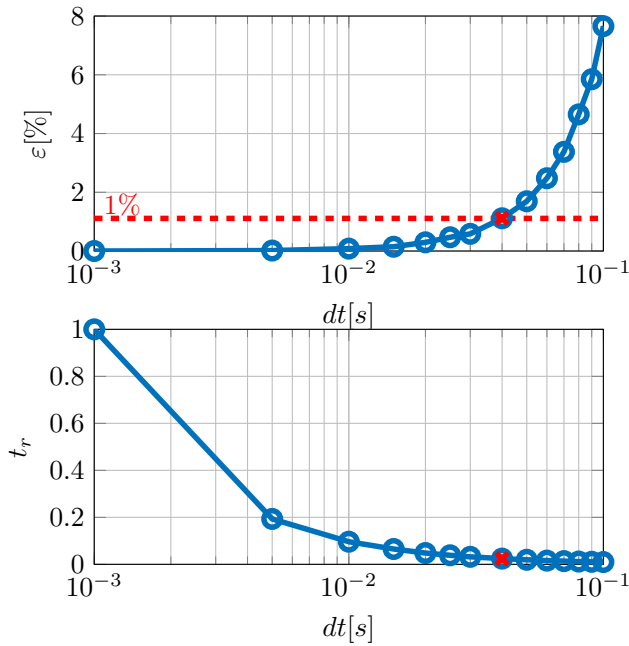

Figure 8. Normalized computational time t_r and mean percentage error ε, defined as in (15), for different time steps dt, for geometry G_1 and wave 3BT2.

Table 3. Normalized computational time (run-time over simulation time), using the nonlinear Froude-Krylov model.

	G_1	G_2
1BT2	4.6	12.5
2BT2	4.6	13.1
3BT2	4.7	13.2

G_2 is larger than the one for G_1. However, other aspects affect the computational time, such as the complexity of the geometry, the displacements of the floater, the value of the integrand, and the ratio between the tolerances of the numerical integration algorithm and the value of the integral. In this work, constant relative and absolute tolerances have been adopted, so that the computing time of small or large quantities may differ significantly. As a possible future improvement of the model, adaptive tolerances (as opposed to constant) may reduce the total computational time without affecting the accuracy.

However, note that the computational time required by the nonlinear FK model also depends on the complexity of the incoming wave representations, namely the number of frequency components (n_ω) (Giorgi and Ringwood, 2018e). Assuming a constant fundamental frequency (depending on the simulated time window), n_ω depends on the cut-off frequency (ω_c). Although low-energy high-frequency content of ordinary panchromatic waves

described by 2 geometrical sections (one hemisphere and one cylinder). On the other hand, G_2 requires considering two cylinders (external surface and moonpool) and one bottom disk. Since the number of FK integrals is proportional to the number of different geometrical sections composing the device, the normalized time for

is usually negligible, it is relevant for the correct reproduction of focused waves, since fully constructive phase interaction of all components is ensured at the focused location to generate the peak. This is one of the reasons why focused waves are particularly challenging to simulate with a nonlinear FK approach, especially for validation purposes, where the ability to replicate the incoming wave is essential. Figure 9 shows how the cut-off frequency, hence the number of frequency components (n_ω), affects the computational time (t_n) and the ability to replicate the peak of the focused wave (η_{max}). The consequent error in reproducing the peak (ε_η) and the computational time are normalized against the case with higher ω_c.
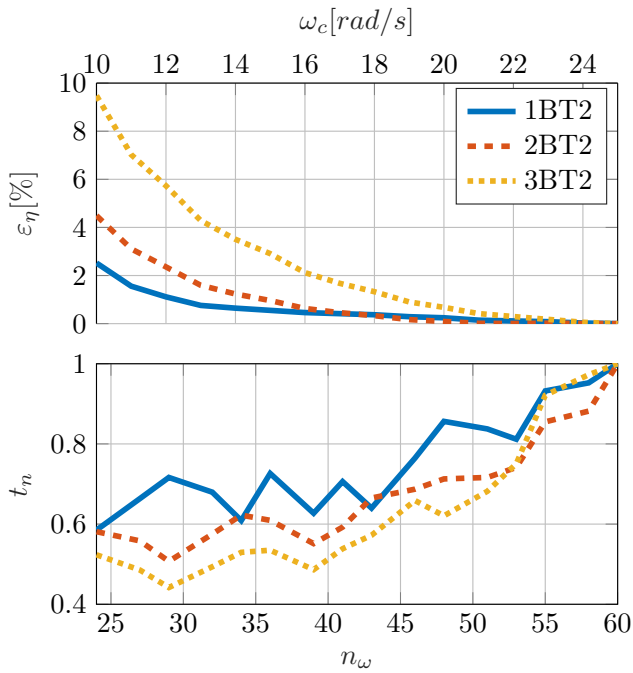
Figure 9. Relative error on the peak of the focused wave surface elevation (ε_η) and normalized computational time (t_n) with respect to the cut-off frequency (ω_c) and number of frequency components (n_ω). Note that there is a one-to-one relationship between ω_c and n_ω. The case with maximum ω_c is used for the normalization.

The impact of ε_η on the response of the device is shown in Fig. 10, for the example of geometry G_2, using a convergence metric ε, defined as in (15). It can be remarked that the surge degree of freedom is the most affected, while heave and pitch are less sensitive to the η_{max}.
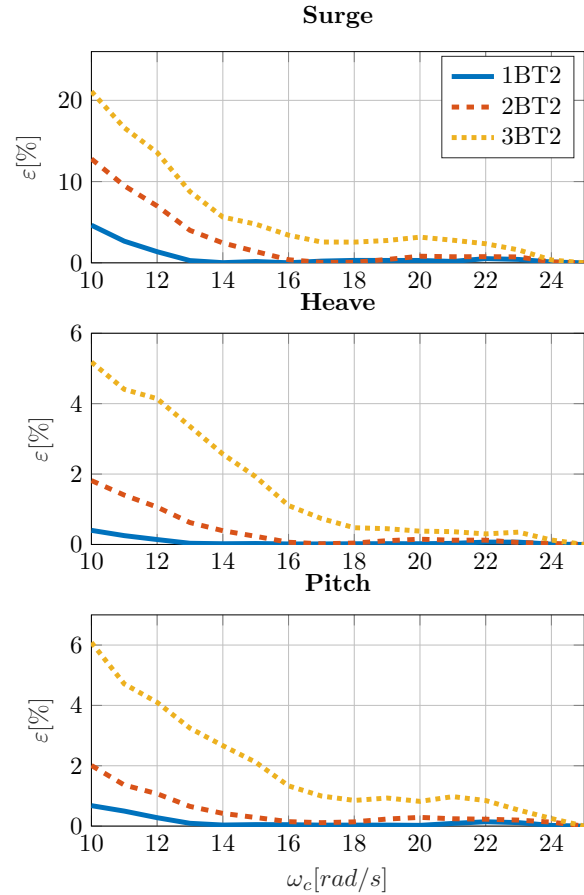

Figure 10. Convergence metric in the surge, heave, and pitch response of geometry G_2, depending on the adopted cut-off frequency ω_c, due to the relative error ε_η, shown in Fig. 9.

The resulting time traces are shown in Figs. 11 and 12, for geometry G_1 and G_2, respectively, and are compared with experimental results (Ransley *et al.*, 2020a,b). The most worthwhile remark is that the profile of the heave response is well captured, both in shape and phase. The only small differences are found in the tail of the response (after the peak) with larger waves, in particular for the floater with the moonpool, likely due to the interaction with the water column, which has not been included as additional degree of freedom in the model. On the other hand, surge and pitch responses are accurate until just before the peak of the wave arrives ($t = 45s$), and diverge from the experimental afterwards. A significant overestimation is found in particular for pitch, especially for geometry G_2. Finally, considering the mooring loads, a reasonably accurate representation is achieved, apart from some deviation in the tail of the response. In fact, in this configuration, mooring loads

depend mainly on the heave displacements, which are accurately represented.

A quantitative description of the accuracy of the reproduction is provided in Table 4, which shows the root mean square error between the simulated and experimental time traces, normalized by the standard deviation of the experimental time trace, as suggested in (Ransley *et al.*, 2020a). It can be remarked that the error in heave remains about constant for increasing wave steepness, for both G1 and G2. Conversely, while the error in pitch decreases with increasing steepness for G1, it shows the opposite trend for G2. This is mainly due to the error in reproducing the tail of the pitch response for G2, with increasing overestimation for steeper waves. On the other hand, for geometry G1, both simulated and experimental pitch response increase with the wave steepness, without decaying in the tail of the time trace. Finally, errors in the mooring tension are due to a combination of all other DoFs, so they show variations for different wave steepness.

Table 4. Normalized root mean square error, normalized by the standard deviation of the experimental time trace.

| | G1 | | |
	11BT2	12BT2	13BT2
Surge	1.351	1.610	1.316
Heave	0.245	0.227	0.234
Pitch	1.243	0.792	0.678
Mooring tension	0.344	0.436	0.476
	G2		
	21BT2	22BT2	23BT2
Surge	0.873	0.759	0.470
Heave	0.281	0.293	0.272
Pitch	1.532	1.696	2.062
Mooring tension	0.365	0.426	0.427

Figure 13 shows the single-sided variance density spectrum of the response of the two geometries for the wave condition of medium steepness (2BT2). Similarly to considerations for the time series, the spectral content is reproduced with reasonable accuracy in heave and mooring load, while surge and especially pitch show a large disagreement. However, Figure 13 shows that the NLFK model is able to articulate super-harmonics due to nonlinear phenomena, although their amplitude and position is seldom matched by experimental data.

The significant overestimation of the pitch response (the least accurate result) has a strong impact in generating discrepancies in other degrees of freedom, in both time and frequency domains. In fact, due to nonlinear kinematics (see Sect. 2.2), such large rotations cause an erroneous decomposition of translational motion from the body-fixed frame to the global frame, favouring surge over heave. This partially explains the overestimation of the surge response and the underestimation of the heave response. The overestimation of the pitch response is partially caused by potential measurement inaccuracies (moments of inertia are particularly challenging quantities to measure), but mainly due to the absence of viscous drag losses in the model as well as the assumption of small interactions between the moonpool and the buoy. In fact, the moonpool and its entrance with sharp edges may cause modifications of the fluid flow that are neglected in this model. Furthermore, surge displacement (coupled with pitch) mainly depends on the mooring force, first order surge force, and the second order drift force. In this model, only drift due to Froude-Krylov forces is considered, while second order diffraction effects are neglected.

However, the author believes that one of the main reasons for inaccurate reproduction of surge and pitch responses lies in the misrepresentation of the pressure field around the body. Linear dispersion relationship is used to compute wave numbers from the Fourier transform of the free surface elevation at $x = 0$. Although the reconstructed time trace of η is exact at $x = 0$, it loses accuracy with distance from the identification coordinate. Similarly, also the pressure field spatial-representation accuracy decreases with x. Forces in surge and pitch are more significantly affected because of their predominant dependence on the pressure difference in the horizontal direction. In this paper, in order to limit the nonlinear dispersion error, the surge displacement is enforced to zero for the computation of the pressure field. However, further investigation is needed to assess what is the impact of nonlinear dispersion in focused waves on nonlinear FK force computation, and eventually introduce a convenient correction.

5. Conclusion

The current stage of development of hydrodynamic models for wave energy applications highlights the urgent need for standardization of modelling techniques and evaluation/comparison metrics, which are essential for developing more confidence and
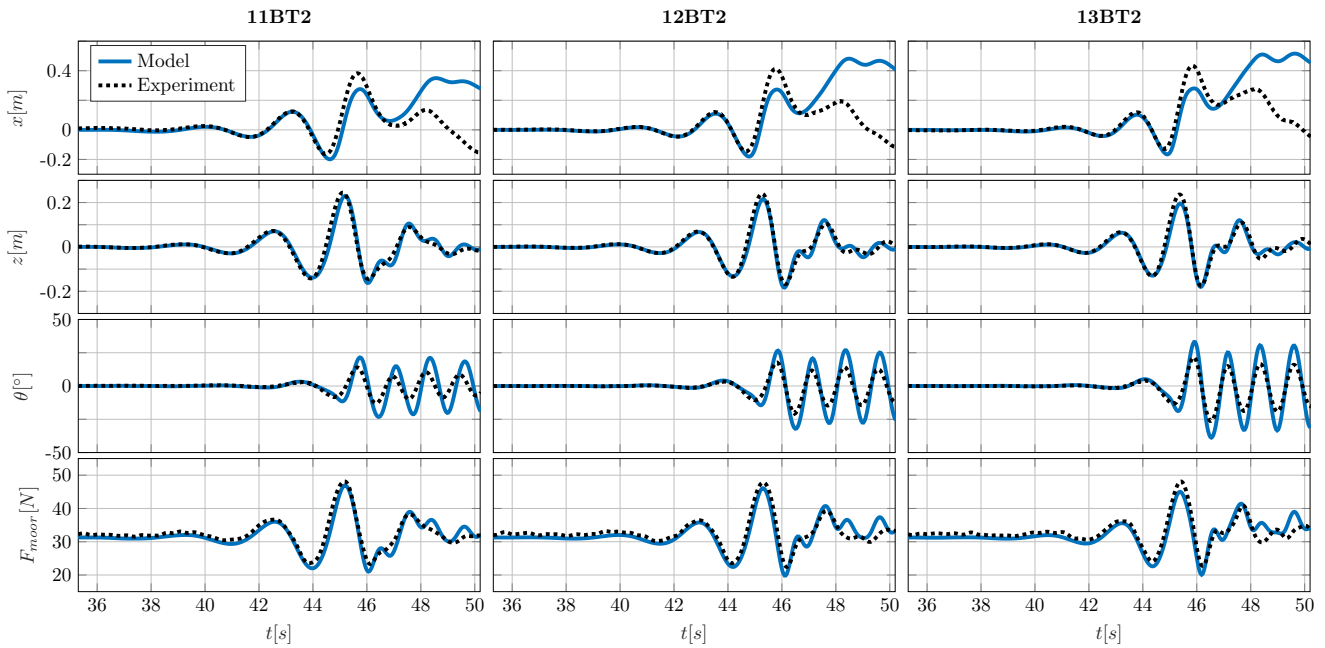
Figure 11. Response of geometry G_1 in surge (x), heave (z), pitch (θ), and mooring load (F_{moor}).
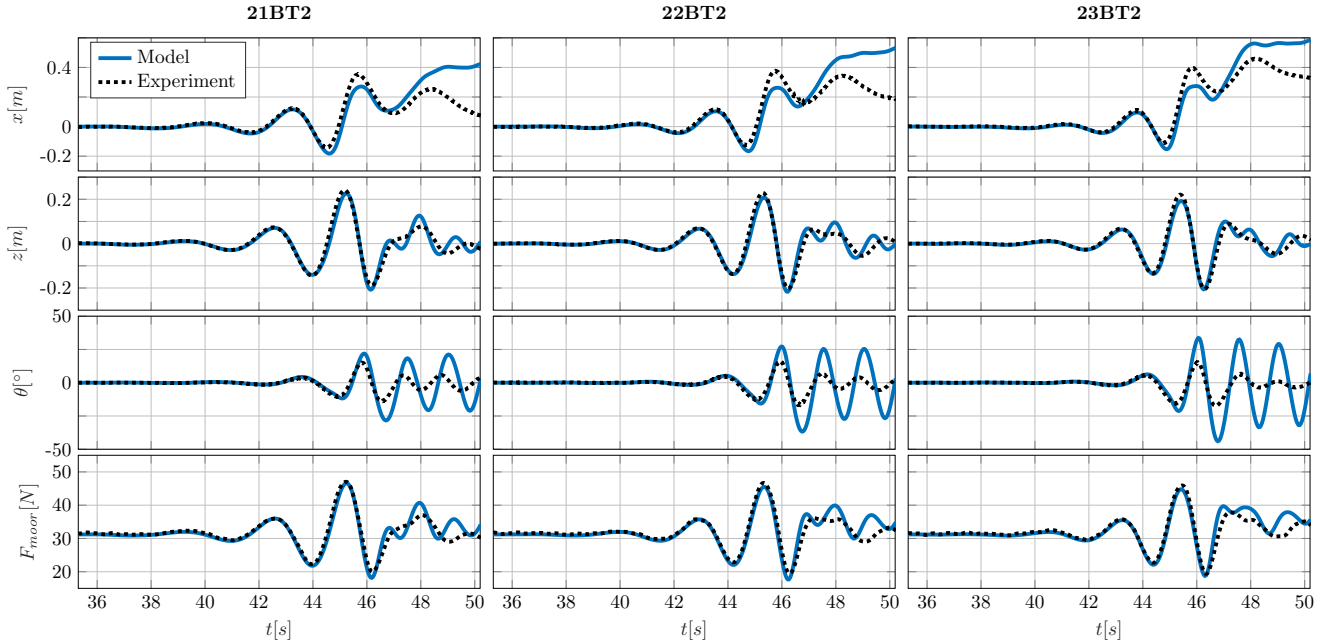

Figure 12. Response of geometry G_2 in surge (x), heave (z), pitch (θ), and mooring load (F_{moor}).

effectiveness of the design process. The CCP-WSI project aims to provide different institutions with common experimental data, in order to implement and compare various modelling techniques for the same test cases. In general, the choice of the model is guided by

the particular requirements of the intended application, especially the accuracy/computational time balance. This paper proposes a model which achieves a medium level of a accuracy, but keeps the run-time close to real-time. Therefore, nonlinear kinematics
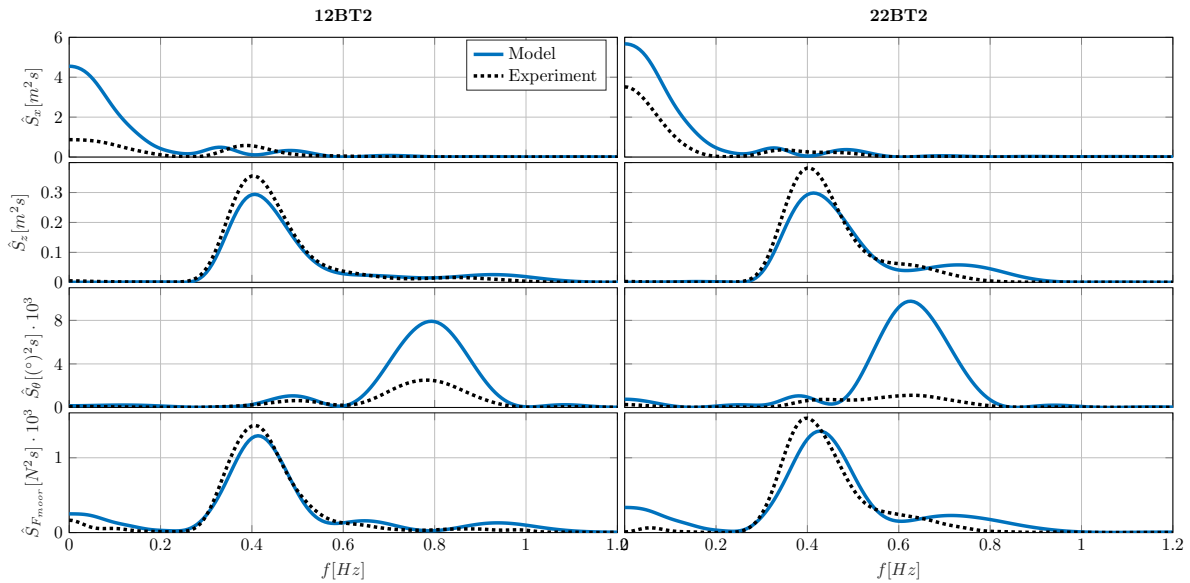
Figure 13. Single-sided variance density spectrum of the response of geometries G_1 (on the left) and G_2 (on the right) in surge ($\hat{S}_x$), heave ($\hat{S}_z$), pitch ($\hat{S}_\theta$), and mooring load ($\hat{S}_{F_{moor}}$).

and nonlinear Froude-Krylov force calculations are implemented, exploiting the axisymmetric shape of the floaters to enhance the computational performance of the model.

Although the focused waves herein considered are representative of medium/extreme conditions, hence outside the natural realm of preferred applicability of a NLFK model, which is operational power-production region, sufficiently accurate results are obtained for the heave response and mooring loads, up to the largest waves. These results have been achieved using one core of an ordinary laptop at a computational time close to real time, various orders of magnitude faster than a common CFD (Computational Fluid Dynamics) simulation.

However, surge and especially pitch responses are relatively poorer, likely due to the absence of viscous drag and the inaccuracy of the representation of the pressure field around the floaters, which is particularly challenging with nonlinear focused waves. A topic for further investigation is the analysis of corrective measures to include the effect of nonlinear propagation in the nonlinear FK framework.

In a nutshell, the NLFK model seems not best in cases where pitch and surge responses to focused waves are of interest, for example in survivability studies. On the other hand, mooring loads and heave response are represented with acceptable accuracy, at a fraction of computational time required by fully-nonlinear models. Since power conversion capabilities of point absorbers wave energy converters are strictly correlated to mooring loads and heave response, the NLFK model finds its best application in control or power optimization studies, where medium fidelity at low computational time is a crucial requirement.

Acknowledgements

REFERENCES

Bhinder MA, Babarit A, Gentaz L and Ferrant P (2011) Assessment of viscous damping via 3d-cfd modelling of a floating wave energy device. In *Proceedings of the 9th European Wave and Tidal Energy Conference*, Southampton.

Clément AH and Ferrant P (1988) Nonlinear Water Waves: IUTAM Symposium, Tokyo Japan, August 25–28, 1987. chap.

Superharmo, Springer Berlin Heidelberg, Berlin, Heidelberg, pp. 423–433.

Davidson J and Costello R (2020) Efficient Nonlinear Hydrodynamic Models for Wave Energy Converter Design — A Scoping Study : 1–65 10.3390/jmse8010035.

Faedo N, Peña-Sanchez Y and Ringwood JV (2018) Finite-Order Hydrodynamic Model Determination for Wave Energy Applications Using Moment-Matching. *Ocean Engineering* **163**: 251–263.

Fossen TI (2011) *Handbook of marine craft hydrodynamics and motion control*. John Wiley & Sons.

Garcia-Rosa PB, Costello R, Dias F and Ringwood JV (2015) Hydrodynamic Modelling Competition: Overview and approaches. In *Proceedings of the ASME 2015 34th International Conference on Ocean, Offshore and Arctic Engineering*.

Gilloteaux JC (2007) *Mouvements de grande amplitude d'un corps flottant en fluide parfait. Application á la recuperation de l'energie des vagues*. PhD thesis, Ecole Centrale de Nantes-ECN.

Giorgi G (2019a) CCP-WSI Blind Test Series 2 : A Nonlinear Froude-Krylov Modelling Approach. In *Proceedings of the 13th European Wave and Tidal Energy Conference, 1-6 September, Naples, Italy*, Naples.

Giorgi G (2019b) CCP-WSI Blind Test Series 3 : A Nonlinear Froude-Krylov Modelling Approach. In *Proceedings of the 29th International Offshore and Polar Engineering Conference, 16-21 June, Honolulu, Hawaii, USA*, Honolulu.

Giorgi G (2019c) Nonlinear Froude-Krylov Matlab demonstration toolbox. 10.5281/zenodo.3667529.

Giorgi G, Gomes RPF, Bracco G and Mattiazzo G (2020) The Effect of Mooring Line Parameters in Inducing Parametric Resonance on the Spar-Buoy Oscillating Water Column Wave Energy Converter. *Journal of Marine Science and Engineering* **8(1)**: 29, 10.3390/JMSE8010029.

Giorgi G and Ringwood JV (2018a) A Compact 6-DoF Nonlinear Wave Energy Device Model for Power Assessment and Control Investigations. *IEEE Transactions on Sustainable Energy* 10.1109/TSTE.2018.2826578.

Giorgi G and Ringwood JV (2018b) Analytical Formulation of Nonlinear Froude-Krylov Forces for Surging-Heaving-Pitching Point Absorbers. In *ASME 2018 37th International Conference on Ocean, Offshore and Arctic Engineering*, Madrid.

Giorgi G and Ringwood JV (2018c) Analytical representation of nonlinear Froude-Krylov forces for 3-DoF point absorbing wave energy devices. *Ocean Engineering* **164(2018)**: 749–759, 10.1016/j.oceaneng.2018.07.020.

Giorgi G and Ringwood JV (2018d) Articulating Parametric Nonlinearities in Computationally Efficient Hydrodynamic Models. In *Proceedings of the 11th IFAC Conferecne on Control Applications in Marine Systems, Robotics, and Vehicles*, Opatija.

Giorgi G and Ringwood JV (2018e) Articulating parametric resonance for an OWC spar buoy in regular and irregular waves. *Journal of Ocean Engineering and Marine Energy* **4(4)**: 311–322, 10.1007/s40722-018-0124-z.

Giorgi G and Ringwood JV (2018f) Relevance of pressure field accuracy for nonlinear Froude–Krylov force calculations for wave energy devices. *Journal of Ocean Engineering and Marine Energy* **4(1)**: 57–71, 10.1007/s40722-017-0107-5.

Penalba M, Mérigaud A, Gilloteaux JC and Ringwood JV (2017) Influence of nonlinear Froude–Krylov forces on the performance of two wave energy points absorbers. *Journal of Ocean Engineering and Marine Energy* **3(3)**: 209–220, 10.1007/s40722-017-0082-x.

Ransley E, Brown S, Hann M, Greaves D, Windt C, Ringwood J, Davidson J, Schmitt P, Yan S, Wang JX, Wang JH, Ma Q, Xie ZH, Giorgi G, Hughes J, Williams A, Masters I, Lin Z, Chen H, Qian L, Ma Z, Causon D, Mingham C, Chen Q, Ding H, Zang J, van Rij J, Yu Y, Tom N, Li Z, Bouscasse B, Ducrozet G and Bingham H (2020a) A blind comparative study of focused wave interactions with floating structures ({CCP-WSI Blind Test Series 2}). *Proceedings of the Institution of Civil Engineers - Engineering and Computational Mechanics* **in review**.

Ransley E, Jones C, Ma Q, Poulter G, Qian L, Tabor G, Yan S, Zang J and Greaves D (2016) *Wave Structure Interaction Computation and Experiment Roadmap Part 1: A Report on the 1st CCP-WSI Focus Group Workshop, PEARL Research Repository*. Technical report, 10.24382/zw9p-t026.

Ransley E, Yan S, Brown S, Hann M, Graham D, Windt C, Schmitt P, Davidson J, Ringwood J, Musiedlak PH, Wang J, Wang J, Ma Q, Xie Z, Zhang N, Zheng X, Giorgi G, Chen H, Lin Z, Qian L, Ma Z, Bai W, Chen Q, Zang J, Ding H, Cheng L, Zheng J, Gu H,

Gong X, Liu Z, Zhuang Y, Wan D, Bingham H and Greaves D (2020b) A blind comparative study of focused wave interactions with floating structures ({CCP-WSI Blind Test Series 3}). *International Journal of Offshore and Polar Engineering* **in review**.

Ransley E, Yan S, Brown S, Mai T, Graham D, Ma Q, Musiedlak PH, Engsig-Karup AP, Eskilsson C, Li Q, Wang J, Xie Z, Sriram V, Stoesser T, Zhuang Y, Li Q, Wan D, Chen G, Chen H, Qian L, Ma Z, Mingham C, Causon D, Gatin I, Jasak H, Vukcevic V, Downie S, Higuera P, Buldakov E, Stagonas D, Chen Q, Zang J and Greaves D (2019) A blind comparative study of focused wave interactions with a fixed FPSO-like structure (CCP-WSI Blind Test Series 1). *International Journal of Offshore and Polar Engineering* **29(2)**: 113–127, 10.17736/ijope.2019.jc748.

Ringwood JV, Merigaud A, Faedo N and Fusco F (2018) Wave Energy Control Systems: Robustness Issues. In *Proceedinds of the IFAC Conference on control Aplications in Marine Systems, Robotics, and Vehicles*.

Salter SH (1974) Wave Power. *Nature* **249(720-724)**: 720–724, 10.1038/249720a0.

Tromans PS, Anaturk AR, Hagemeijer P and Others (1991) A new model for the kinematics of large ocean waves-application as a design wave. In *The First International Offshore and Polar Engineering Conference*, International Society of Offshore and Polar Engineers.

WAMIT Inc. MIT (2014) User Manual Wamit .

Wang H, Somayajula A, Falzarano J and Xie Z (2019) Development of a Blended Time-Domain Program for Predicting the Motions of a Wave Energy Structure. *Journal of Marine Science and Engineering* **8(1)**: 1, 10.3390/jmse8010001.

Wendt F, Nielsen K, Yu Yh, Bingham H, Eskilsson C, Kramer B, Babarit A, Bunnik T, Costello R, Crowley S, Giorgi G, Giorgi S, Girardin S and Greaves D (2019) Ocean Energy Systems Wave Energy Modeling Task : Modeling , Verification , and Validation of Wave Energy Converters. *Journal of Marine Science and Engineering* : 1–22 10.3390/jmse7110379.